Large and massive neutron stars: Implications for the sound speed within QCD of dense matter

Christian Drischler[1,*], Sophia Han (韩君)[2,3,†] and Sanjay Reddy[2,‡]

[1]*Facility for Rare Isotope Beams, Michigan State University, East Lansing, Michigan 48824, USA*
[2]*Institute for Nuclear Theory, University of Washington, Seattle, Washington 98195, USA*
[3]*Department of Physics, University of California, Berkeley, California 94720, USA*

(Received 28 October 2021; accepted 10 March 2022; published 28 March 2022)

The NASA telescope *NICER* has recently measured x-ray emissions from the heaviest of the precisely known two-solar mass neutron stars, PSR J0740 + 6620. Analysis of the data [Astrophys. J. Lett. **918**, L28 (2021), Astrophys. J. Lett. **918**, L27 (2021)] suggests that PSR J0740 + 6620 has a radius in the range of $R_{2.0} \approx (11.4\text{–}16.1)$ km at the 68% credibility level. In this article, we study the implications of this analysis for the sound speed in the high-density inner cores by using recent chiral effective field theory (χEFT) calculations of the equation of state at next-to-next-to-next-to-leading order to describe outer regions of the star at modest density. We find that the lower bound on the maximum speed of sound in the inner core, $\min\{c^2_{s,\max}\}$, increases rapidly with the radius of massive neutron stars. If χEFT remains an efficient expansion for nuclear interactions up to about twice the nuclear saturation density, $R_{2.0} \geqslant 13$ km requires $\min\{c^2_{s,\max}\} \geqslant 0.562$ and 0.442 at the 68% and 95% credibility level, respectively.

DOI: 10.1103/PhysRevC.105.035808

I. INTRODUCTION

The dedicated NASA x-ray telescope *Neutron Star Interior Composition Explorer* (*NICER*) has recently measured soft-x-ray emissions from hotspots on the surface of the millisecond pulsar PSR J0740 + 6620—the heaviest of the precisely known two-solar-mass neutron stars, $M = 2.08 \pm 0.07\,\mathrm{M}_\odot$ [1,2]. Independent analyses of the *NICER* and *XMM-Newton* data combined suggest that PSR J0740 + 6620 also has a large radius in the range of ≈(11.4–16.1) km at the 68% credibility level. Specifically, the Maryland-Illinois group inferred (12.2–16.1) km [3], while the x-ray Pulse Simulation and Inference (XPSI) group obtained with (11.4–13.7) km [4] statistically consistent but somewhat smaller radii.[1] These analyses indicate for the first time, despite their significant uncertainties, that radii of massive neutron stars can be large. Specifically, they motivate a scenario with $R_{2.0} > R_{1.4}$, where $R_{2.0}$ and $R_{1.4}$ are the radii of neutron stars with masses $M = 2.0\,\mathrm{M}_\odot$ and $1.4\,\mathrm{M}_\odot$, respectively. A large $R_{2.0} \gtrsim 13$ km would have profound implications for the properties of the dense matter equation of state (EOS) in neutron-star cores as well as the composition and phases within quantum chromodynamics of dense matter (dense QCD) at low temperatures. In this article, we explore some of these implications for the sound speed of large and massive neutron stars.

Astronomical observations can provide important constraints on the EOS since neutron star properties such as masses, radii, and tidal deformabilities are sensitive to the EOS in the (baryon) density regime $n_\mathrm{B} \approx (2\text{–}4)\,n_\mathrm{sat}$. Here, $n_\mathrm{sat} = 0.16\ \mathrm{fm}^{-3}$ denotes the canonical value for the empirical nuclear saturation density, a typical density in heavy atomic nuclei. In particular, radio observations have provided precise mass measurements of three neutron stars with masses $\approx 2\,\mathrm{M}_\odot$ [1,2,5,6]. Such high masses require high matter pressure in the neutron-star core, disfavoring strong first-order phase transitions in this density range. Furthermore, the first direct gravitational wave (GW) detection from the binary neutron-star merger GW170817 provided stringent constraints on the tidal deformability of neutron stars with canonical masses $\approx 1.4\,\mathrm{M}_\odot$ [7–9]. The firm upper bound on the tidal deformability inferred from GW170817 has indicated a relatively small radius $\lesssim$13.4 km [7,10–12] for $\approx 1.4\,\mathrm{M}_\odot$ stars, suggesting that the pressure of matter at the densities encountered in the outer core is low. Analysis of x-ray observations of surface thermal emissions from quiescent neutron stars in low-mass x-ray binaries (LMXBs) also favor small radii in the range (10–12) km [13,14], although the systematic uncertainties are still large [15,16]. When combined, radio and GW observations favor a rapid transition from low to high pressures toward the inner core. In natural units this corresponds to sound speeds $c_s \geqslant \sqrt{1/3}$ because $c_s^2 = \partial P(\varepsilon)/\partial\varepsilon$ is the derivative of the pressure $P(\varepsilon)$ with respect to the energy density ε including rest mass contributions [17,18].

The purpose of this article is to determine the minimum sound speed in the neutron-star core required to support radii in the range of $R_{2.0} \approx (11.4\text{–}16.1)$ km. To this end, we use recent microscopic EOS constraints [19–22] derived from chiral effective field theory (χEFT) up to next-to-next-to-next-to-leading order (N^{3}LO) with correlated χEFT

*drischler@frib.msu.edu
†sjhan@berkeley.edu
‡sareddy@uw.edu

[1]The XPSI group [4] used a larger calibration uncertainty compared with the Maryland-Illinois group [3] which permits lower inferred radii, and also a hard upper limit (inferred from theoretical nuclear models) such that the prior support is zero for radii greater than 16 km.

truncation errors [23] quantified. These errors, which arise due to truncating the χEFT expansion at a finite order in practice, are important to quantify as they can be significant for $n_B \gtrsim n_{sat}$, even at N^{3}LO in the χEFT expansion (see, e.g., Ref. [24] for a recent review article).

The remainder of this article is organized as follows: We discuss in Sec. II the importance of theoretical calculations and experimental constraints on the nuclear matter EOS in the density region of $(1–2)\,n_{sat}$. Section III assesses how the current uncertainties in microscopic EOS calculations up to $\approx 2\,n_{sat}$ impact the interpretation of neutron-star observations about the sound speeds of high-density matter. In Sec. IV, we conclude by discussing the implications of high sound speeds and large neutron-star radii for dense-matter physics and multimessenger astronomy. We use natural units in which $\hbar = c = 1$.

II. EQUATION OF STATE OF THE OUTER CORE

In a recent article [25], we showed how upper and lower bounds on the neutron-star radius of any mass can be derived from microscopic EOS calculations up to some density n_c; typically, $n_c \lesssim 2.0\,n_{sat}$. Matching these microscopic calculations at $n_B = n_c$ to a maximally stiff EOS characterized by a constant sound speed $c^2_{s,match} \leqslant 1$ for $n_B \gtrsim n_c$ allows one to obtain robust upper and lower bounds on the neutron-star radius. If the pressure and energy density are matched continuously at $n_B = n_c$, the maximum radius associated with that EOS can be inferred; whereas matching with a maximal finite discontinuity in the energy density specified by an assumed lower bound on M_{max} determines the minimum radius. Here, we extend this work to provide a lower bound on the maximum speed of sound, $\min\{c^2_{s,max}\}$, reached in the core of PSR J0740 + 6620 for a given radius $R_{2.0}$ in the range of the recent *NICER* measurement.

Following the strategy discussed in Ref. [25], we construct the neutron-star EOS from low to high densities by matching EOSs defined in three different density regions. At low densities, $n_B \leqslant 0.5\,n_{sat}$, we use the standard crust EOS derived by Baym, Pethick, and Sutherland [32] and Negele and Vautherin [31]. At intermediate densities, $0.5\,n_{sat} < n_B \leqslant n_c$, we interpolate microscopic calculations of the EOS in pure neutron matter (PNM) and symmetric nuclear matter (SNM) to beta-equilibrated matter, i.e., neutron-star matter (NSM), using the standard quadratic expansion of the EOS's isospin dependence. Explicit calculations of isospin-asymmetric matter based on χEFT nucleon-nucleon (NN) and three-nucleon ($3N$) interactions have shown that the standard quadratic expansion is a reasonable approximation [33–38]. We refer to this region as the outer core.

Specifically, in the outer core, we consider the microscopic constraints on the zero-temperature EOS in PNM and SNM obtained in Refs. [19–21] by high-order many-body perturbation theory (MBPT) calculations. These many-body calculations with nonlocal NN and $3N$ interactions at the same order in the χEFT expansion have improved previous state-of-the-art MBPT results [39–41], allow for estimating EFT truncation errors up to N^{3}LO and were recently used in the first statistical analysis of correlated EFT truncation errors in nuclear matter [21,22]. Furthermore, the underlying N^{2}LO and N^{3}LO interactions exhibit reasonable nuclear saturation properties in SNM (as the leading short-range $3N$ forces were adjusted to the empirical saturation point) and predict the nuclear symmetry energy evaluated at n_{sat} and its slope parameter in excellent agreement with experimental constraints (see Fig. 2 in Ref. [21]). Similar to other χEFT calculations, the slope parameter is predicted to be significantly lower than the mean value of the recent PREX–II-informed constraint obtained from covariant energy density functionals [42], $L = (106 \pm 37)$ MeV. However, the microscopic EOS used here is consistent at the 68% level with the PREX–II-informed constraint due to the large experimental uncertainties. It should also be noted that the PREX–II measurement of the ^{208}Pb neutron skin is in tension with constraints from the ^{208}Pb dipole polarizability, which has not yet been reconciled [43,44].

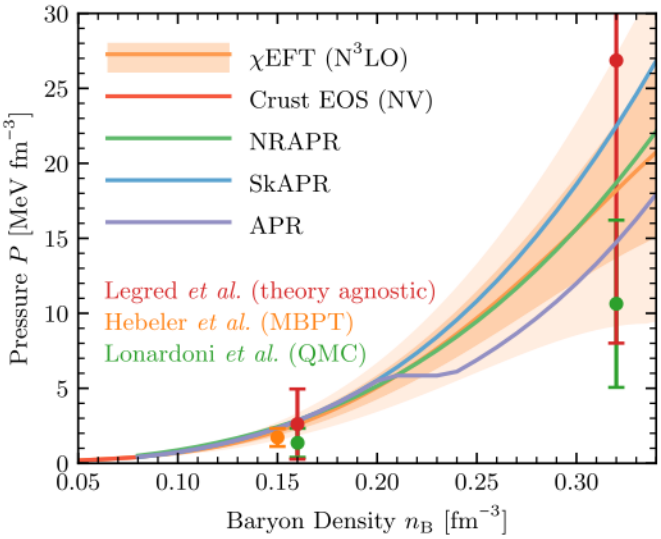

FIG. 1. The pressure P as a function of the baryon density n_B in neutron-star matter. The uncertainty bands (dark: 1σ, light: 2σ) were derived in Ref. [25] by using the N^{3}LO results obtained in Refs. [21,22] for the interaction with the momentum cutoff 500 MeV ["GP–B (500 MeV)"]. The error bars show the microscopic constraints from Hebeler *et al.* [26] (based on lower-order MBPT calculations) and Lonardoni *et al.* [27] (based on QMC calculations) as well as the theory-agnostic constraints from neutron-star observation by Legred *et al.* [28]. The green, blue, and purple lines depict the phenomenological EOSs NRAPR, SkAPR, and APR in beta equilibrium [29,30], respectively. Note that the APR EOS involves a first-order transition into a pion condensate around $1.3\,n_{sat}$. At $n_B \leqslant 0.08$ fm^{-3}, we also show the crust EOS by Negele and Vautherin [31] (NV, red line).

Figure 1 shows the resulting pressure $P(n_B)$ at N^{3}LO in neutron-star matter as a function of the baryon density n_B. The mean value is depicted by the orange solid line, while the dark (light) orange shaded regions correspond to the 1σ (2σ) confidence interval. For comparison, we also show the pressures predicted by the phenomenological EOSs NRAPR (green line), SkAPR (blue line), and APR (purple line), as well as microscopic constraints obtained from MBPT [26] (orange error bar) and quantum Monte Carlo (QMC) calculations (green error bars) [27]. The microscopic calculations used in this work tend to predict somewhat stiffer EOSs compared with other

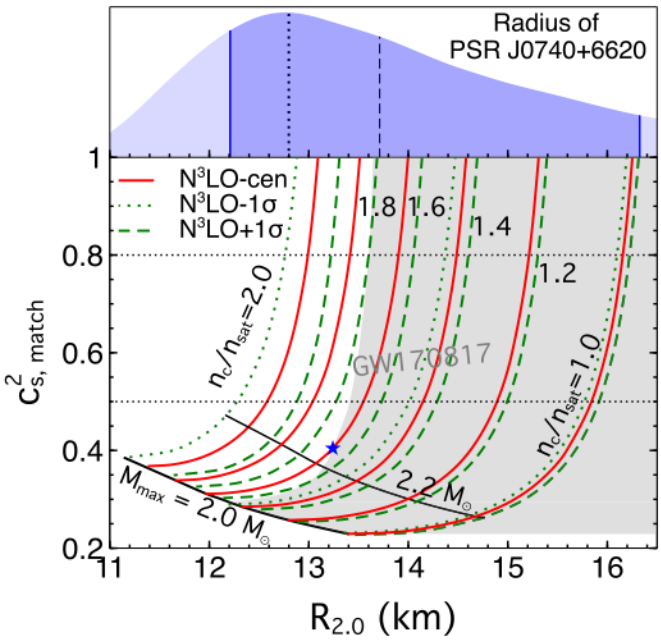

FIG. 2. The top panel shows the joint probability distribution (on an arbitrary scale) for the radius of PSR J0740 + 6620 as inferred from *NICER* and *XMM-Newton* data [3]. The median at $R_{2.0} =$ 13.713 km (dashed vertical line) and mode at $R_{2.0} = 12.850$ km (dotted vertical line) are shown, and the 68% confidence interval centered around the median is depicted by the dark blue shading, $R_{2.0} = (12.209–16.326)$ km. See also Fig. 1 and Table 3 in Ref. [3]. The bottom panel: $R_{2.0}$-$c^2_{s,\mathrm{match}}$ plot for N^{3}LO $\pm 1\sigma$ EOSs in Fig. 1 up to chosen matching densities in the range $n_c = (1–2)\,n_{\mathrm{sat}}$, assuming there is no additional softening induced by a first-order phase transition at such low densities. The gray-shaded region is excluded by the binary tidal deformability constraint $\tilde{\Lambda}_{1.186} \leqslant 720$ from GW170817 at the 90% credibility level [45] for the N^{3}LO-cen EOS. The blue asterisk represents the intersection between the GW170817 boundary and the $n_c = 1.6\,n_{\mathrm{sat}}$ curve for N^{3}LO-cen, which corresponds to the maximum $R_{2.0}$ consistent with GW constraint if the N^{3}LO-cen EOS is valid up to $n_c = 1.6\,n_{\mathrm{sat}}$ (see discussion in Sec. III B). The two horizontal dotted lines indicate $c_s^2 = 0.5$ and 0.8.

recent microscopic calculations, but still lie on the softer side of the theory-agnostic constraints by Legred *et al.* [28] (red error bars). For instance, in PNM at N^{2}LO, the EOS considered here predicts $P(2\,n_{\mathrm{sat}}) \approx (20.6 \pm 6.6)$ MeV fm^{-3} at the 1σ confidence level, while state-of-the-art QMC calculations based on a different set of local χEFT NN and $3N$ interactions obtained $P(2\,n_{\mathrm{sat}}) \approx (15.1 \pm 4.7)$ MeV fm^{-3} (see Table 2 in Ref. [18]). The overall trend that the microscopic calculations used in this work tend to predict somewhat stiffer EOSs is still present at N^{3}LO, although less pronounced, where the MBPT calculations predict $P(2\,n_{\mathrm{sat}}) \approx (18.5 \pm 5.2)$ MeV fm^{-3} in PNM.

III. SPEED OF SOUND IN THE INNER CORE

A. Limits on the high-density speed of sound from M_{max} and $R_{2.0}$ considerations

At higher densities $n_{\mathrm{B}} > n_c$, we parametrize the inner core by using a maximally stiff EOS with a constant sound speed

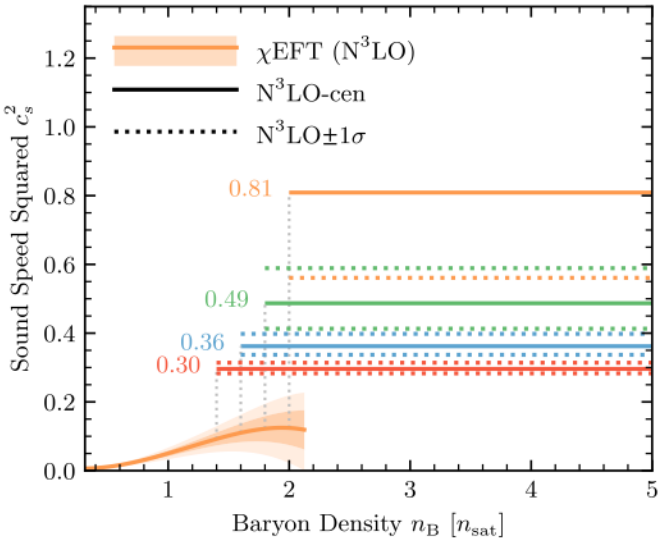

FIG. 3. Sound speed profiles $c_s^2(n_{\mathrm{B}})$ for N^{3}LO-NSM EOSs at low densities (Fig. 1), and for matched EOSs with different values of $c^2_{s,\mathrm{match}}$ at higher densities $n_{\mathrm{B}} \geqslant n_c$ corresponding to $R_{2.0} = 13$ km in Fig. 2 (solid for the central value and dashed for $\pm 1\sigma$ uncertainties); see also Table I.

$c^2_{s,\mathrm{match}} \leqslant 1$, which is stiffer than all other EOSs that have their maximum c_s^2 below $c^2_{s,\mathrm{match}}$, and when matched smoothly to the outer core, it leads to both the largest neutron-star radii and the highest M_{max} (see Ref. [25] for details). Consequently, $c^2_{s,\mathrm{match}}$ represents the smallest possible $c^2_{s,\mathrm{max}}$ for any realistic high-density EOSs to achieve a specific value of neutron-star radius and/or M_{max}.

We solve the Tolman–Oppenheimer–Volkoff (TOV) equations [46,47] of hydrostatic equilibrium for nonrotating neutron stars for a set of EOSs with different $(c^2_{s,\mathrm{match}}, n_c)$ to map the minimum speed of sound in the core $\min\{c^2_{s,\mathrm{max}}\} = c^2_{s,\mathrm{match}}(R_{2.0}, n_c)$ needed to support a neutron star with a given radius $R_{2.0}$ for matching density n_c. Since rotational effects alter the equatorial radius only when the neutron-star spin frequency $\nu \simeq \nu_{\mathrm{K}}$, where $\nu_{\mathrm{K}} \approx 1076\ \mathrm{Hz}(R_{2.0}/12\ \mathrm{km})^{-3/2}$ is the Keplerian frequency [48,49], we neglect the effect of rotation on neutron-star structure given that the observed spin frequency of PSR J0740 + 6620 $\nu = 346.5$ Hz is small.

Figure 2 shows our central results for χEFT-NSM EOS at N^{3}LO with $\pm 1\sigma$ uncertainties (Fig. 1), supplemented with the radius measurement of PSR J0740 + 6620 reported by Miller *et al.* [3] in the top panel.[2] As examples, select combinations of n_c and $c^2_{s,\mathrm{match}}$ that lead to $R_{2.0} = 13$ km are given in Fig. 3 and Table I, and results for χEFT-N^{3}LO $\pm 2\sigma$ are shown in Fig. 4. We choose the different matching densities in the range $n_c = (1–2)\,n_{\mathrm{sat}}$ optimized for large values of $R_{2.0}$ ($n_c > 2.0\,n_{\mathrm{sat}}$ gives rise to even smaller $R_{2.0}$).

[2]We show the radius distribution function from Miller *et al.* [3] because it is based on a more agnostic prior (allowing neutron-star radii >16 km) than the one in Ref. [4]. This choice does not affect our calculations or the derived lower bounds on $c^2_{s,\mathrm{max}}$.

TABLE I. Required stiffening condition (increase in c_s^2) at high densities above n_c for χEFT-NSM EOSs (N^{3}LO-cen and $\pm1\sigma$) to reach $R_{2.0} = 13$ km (see Fig. 2); for the full sound speed profiles, see Fig. 3.

$R_{2.0} = 13$ km	$[c^2_{s,\mathrm{match}},\ c_s^2(n_\mathrm{B} = n_c),\ \Delta c_s^2(n_\mathrm{B} \geqslant n_c)]$		
n_c/n_sat	-1σ	N^{3}LO-cen	$+1\sigma$
2.0	Acausal[a]	[0.809, 0.124, 0.685]	[0.562, 0.173, 0.389]
1.8	[0.589, 0.084, 0.505]	[0.487, 0.122, 0.365]	[0.413, 0.158, 0.255]
1.6	[0.398, 0.083, 0.315]	[0.364, 0.110, 0.254]	[0.335, 0.137, 0.198]
1.4[b]	[0.314, 0.073, 0.241]	[0.296, 0.092, 0.204]	[0.283, 0.111, 0.172]

[a]For the N^{3}LO-1σ EOS, the maximum $R_{2.0}$ is 12.88 km (by setting $c^2_{s,\mathrm{match}} = 1$).
[b]Incompatible with GW170817 in the absence of a phase transition.

We find that $\min\{c^2_{s,\mathrm{max}}\}$ rises more rapidly with $R_{2.0}$ if the matching density n_c is fixed at a higher value. Assuming the central χEFT-N^{3}LO EOS (denoted as N^{3}LO-cen hereafter) is valid up to $n_c = 2.0\,n_\mathrm{sat}$ ($1.8\,n_\mathrm{sat}$), represented by the two leftmost solid red curves in Fig. 2, an increase in $R_{2.0}$ from 12.6 to 13.1 km would require $\min\{c^2_{s,\mathrm{max}}\}$ to increase from $\approx$0.5 (0.39) to $\approx$1.0 (0.53). In consequence, for large values of $R_{2.0}$ the required increase in c_s^2 (i.e., the rapid stiffening of the EOS) over the density range close to n_c is substantial. This is evident from Fig. 3 and Table I, where we demonstrate the variance in c_s^2 for EOSs that correspond to $R_{2.0} = 13$ km. Although the situation is ameliorated for the stiffer $+1\sigma$ EOS and for smaller values of n_c, magnitudes of the jump Δc_s^2 indicate that, above n_c, an unusual stiffening in the EOS compared with what χEFT predicts toward high density is necessary, in particular given the fact that c_s^2 rises at a much smaller rate when approaching $\approx 2\,n_\mathrm{sat}$ from below.

For a given n_c, the stiffer $+1\sigma$ and $+2\sigma$ EOSs (green dashed curves in Figs. 2 and 4) result in smaller values of $\min\{c^2_{s,\mathrm{max}}\}$, and therefore provide conservative estimates about the lower bound on the maximum core speed of sound. Considering the stiffest EOS compatible with χEFT-N^{3}LO at the 2σ level (see the right panel in Fig. 4), the largest possible $R_{2.0}$ limited by causality is then $\approx$13.53 km (13.87 km) for $n_c = 2.0\,n_\mathrm{sat}$ ($1.8\,n_\mathrm{sat}$) (where the green dashed curves intersect with the upper y axis), and a measurement of $R_{2.0} \geqslant 13$ km indicates $\min\{c^2_{s,\mathrm{max}}\} \geqslant 0.42$ (0.35), which violates the conformal bound $c_s^2 \leqslant 1/3$ [11,17,18,50]. Note that, at this stage, we have not yet taken into account tidal deformability constraints from GW170817 [45] (represented by the gray regions that are excluded) which dominate the upper limit on the stiffness or pressure of EOS at intermediate densities (2–3) n_sat [11,28].

Our conclusion that a high sound speed is required in the inner core of PSR J0740 + 6620, if neutron-star radii $\gtrsim$13 km are realistic, is a direct consequence of the modest pressures predicted at $n_\mathrm{B} \approx$ (1–2) n_sat. This is not unique to the EOS used here. As indicated in Fig. 1, most microscopic calculations to date find similar soft neutron-rich matter EOSs. Within the uncertainties, the pressures in neutron-star matter predicted by χEFT calculations are not increasing rapidly enough at $\approx 2\,n_\mathrm{sat}$. But the microscopic EOS used in this work is stiffer than other EOS constraints from χEFT. Hence, our constraints on the minimum core sound speed (at N^{3}LO) are conservative, as other microscopic calculations would predict a higher lower bound.

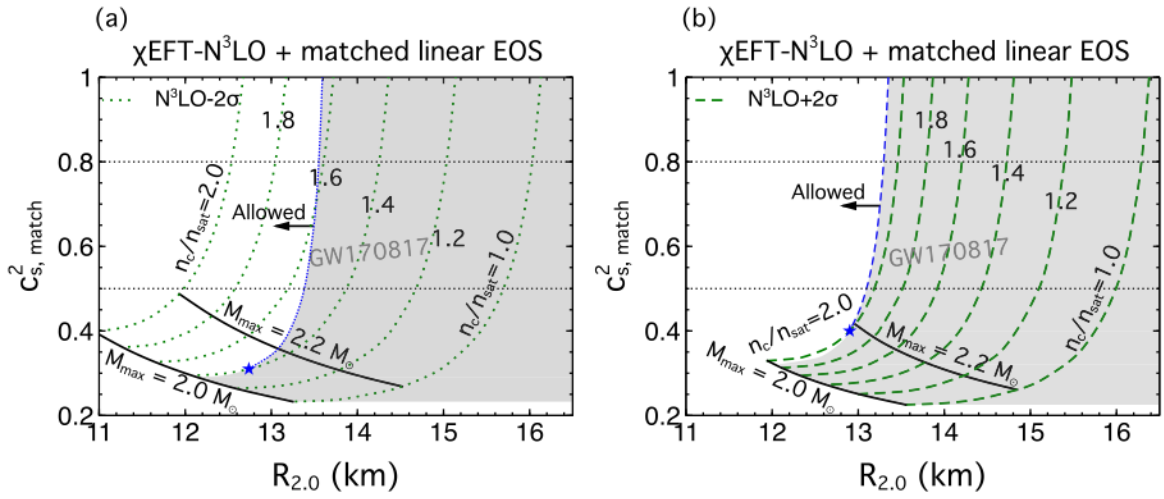

FIG. 4. Similar to Fig. 2 but for the N^{3}LO $\pm$ 2σ EOSs applied at low densities 1–2 n_sat. Examples of the revised $R_{2.0}$-$c^2_{s,\mathrm{match}}$ relation (and the $\min\{c^2_{s,\mathrm{max}}\}$ determined thereafter) permitting phase transitions $\Delta\varepsilon_\mathrm{m} \geqslant 0$ include the blue dotted curve in panel (a) for $n_c = 1.4\,n_\mathrm{sat}$ with N^{3}LO -2σ, and the blue dashed curve in panel (b) for $n_c = 2.0\,n_\mathrm{sat}$ with N^{3}LO $+2\sigma$. The blue asterisks indicate where the strength of the phase transition decreases to zero, i.e., no finite discontinuities in the EOS, and the revised n_c curve (blue dotted and blue dashed) is smoothly joined to the part of the original n_c curve that lies outside the gray region (green dotted and green dashed).

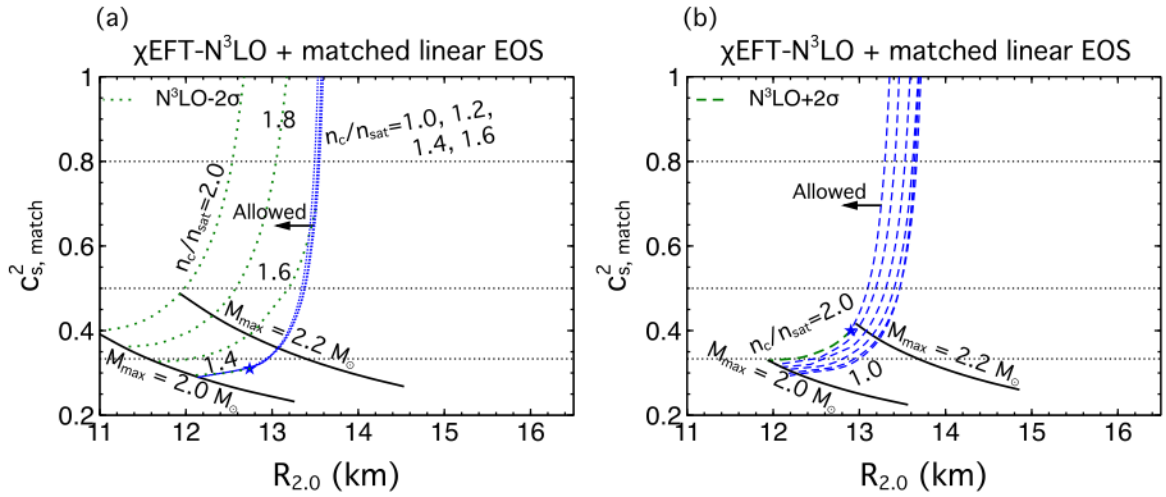

FIG. 5. Revised GW170817 boundaries for the $\pm 2\sigma$ EOSs with various values of n_c ($n_c = 1.0$, 1.2, 1.4, and $1.6\,n_{\rm sat}$ in panel (a) and $n_c = 1.0$, 1.2, 1.4, 1.6, 1.8, and $2.0\,n_{\rm sat}$ in panel (b), from right to left) in the presence of a phase transition, represented by the blue dotted and blue dashed curves, which step into the gray excluded regions shown in Fig. 4. For such low matching densities (or early stiffening in the EOS) and accordingly large $R_{2.0}$ to be compatible with $\tilde{\Lambda}_{1.186} \leqslant 720$, a phase transition is needed and the inferred $\min\{c^2_{s,\rm max}\}$ for a given $R_{2.0}$ is higher because of the (local) extra softening induced at the transition. For comparison, the conformal limit $c_s^2 = 1/3$ is also indicated (bottom dotted horizontal line).

There also exists a generic lower bound on $\min\{c^2_{s,\rm max}\}$ determined by requiring that the maximum mass of neutron stars is at least $\approx 2\,{\rm M}_\odot$, as indicated in Figs. 2 and 4 by the black solid boundaries where all colored curves end. Here, we choose $M_{\rm max} = 2.0\,{\rm M}_\odot$ and $2.2\,{\rm M}_\odot$ to display the trend. A smaller $M_{\rm max}$ is accompanied by a smaller $R_{2.0}$, and for any assumed lower bound on $M_{\rm max}$, the corresponding lower bound on $\min\{c^2_{s,\rm max}\}$ increases when n_c increases, moving from the right to the left along the black solid boundaries.

B. Accommodating GW170817 constraints and the role of phase transitions

In this section, we focus on the compatibility between small tidal deformability constraints from GW170817 and possible (large) radius constraints on massive neutron stars. Using the standard PhenomPNRT model, the binary chirp mass $\mathcal{M} = 1.186 \pm 0.001\,{\rm M}_\odot$ and the binary tidal deformability $\tilde{\Lambda}_{1.186} \leqslant 720$ (90% credibility level) of GW170817 were obtained by gravitational waveform fitting [45,51]. We briefly describe how the upper bound on $\tilde{\Lambda}$ translates into constraints on the high-density EOS parameters and effectively the inferred $R_{2.0}$. We also investigate the modification to the minimally required core sound speed $\min\{c^2_{s,\rm max}\}$ when GW170817 is taken into account, with or without sharp phase transitions, i.e., finite discontinuities in the energy density $\Delta\varepsilon$ in the EOS.

Figure 2 shows the gray-shaded region on the $R_{2.0}$-$c^2_{s,\rm match}$ plane, which is excluded by GW170817 ($\tilde{\Lambda}_{1.186} \leqslant 720$, N^{3}LO-cen EOS), assuming that no phase transition occurs at $n_{\rm B} = (1\text{–}2)\,n_{\rm sat}$. It is clear that low matching densities $n_c \lesssim 1.5\,n_{\rm sat}$ disagree with the GW data; for a given n_c, the largest possible $R_{2.0}$ consistent with small tidal deformabilities observed is therefore determined by the intersection between the GW170817 boundary and the corresponding n_c contour. For $n_c = 1.6\,n_{\rm sat}$, this value is $R_{2.0} \approx 13.24$ km (blue asterisk) alongside a high speed of sound in the core $c^2_{s,\rm match} \approx 0.404$. Tracking the GW170817 boundary upwards, both n_c and $R_{2.0}$ grow gradually with a steep increase in $c^2_{s,\rm match}$.

If the low-density EOS is softer, it is relatively simple to meet the GW170817 constraints, which allows more space for matching at smaller n_c; see the gray region in Fig. 4(a) for the N^{3}LO $-$ 2σ EOS compared with that in Fig. 2. On the other hand, for the stiffest N^{3}LO + 2σ EOS, the tension with the GW170817 constraints is more severe and matching densities $\lesssim 2.0\,n_{\rm sat}$ are almost entirely ruled out [see Fig. 4(b)].

We turn now to the discussion of incorporating effects from sharp phase transitions. For instance, in Fig. 4(a), the original $n_c = 1.4\,n_{\rm sat}$ curve (green dotted lines) without additional softening in the EOS mostly lies inside the gray region (except the short piece below the blue asterisk), which is incompatible with GW170817, i.e., violating $\tilde{\Lambda}_{1.186} \leqslant 720$, and such small values of n_c should be considered nearly excluded. However, by introducing a finite density discontinuity $\Delta\varepsilon_{\rm m}$ at $n_{\rm B} = n_c$, smaller tidal deformabilities at masses relevant to GW170817 become feasible, and the resulting $c^2_{s,\rm match}$-$R_{2.0}$ relation for $n_c = 1.4\,n_{\rm sat}$ (that allows a phase transition) determined by the limiting case $\tilde{\Lambda}_{1.186} = 720$ is shifted toward the left (blue dotted lines), compared with the previous curve that lies inside the gray excluded region (green dotted lines). Interestingly, this updated $n_c = 1.4\,n_{\rm sat}$ curve (blue dotted line) closely tracks the original GW170817 boundary, the edge of the gray region, which assumes no phase transition for all n_c.

To further explore modifications that sharp phase transitions at different matching densities brought about to the GW170817 boundary, we display in Fig. 5 the associated curves for which $n_c \leqslant 1.6\,n_{\rm sat}$ [Fig. 5(a), N^{3}LO $-$ 2σ EOS] and $n_c \leqslant 2.0\,n_{\rm sat}$ [Fig. 5(b), N^{3}LO + 2σ EOS], respectively. We find that smaller n_c allows slightly larger $R_{2.0}$ with the revised boundary moving toward the right on the $R_{2.0}$-$c^2_{s,\rm match}$

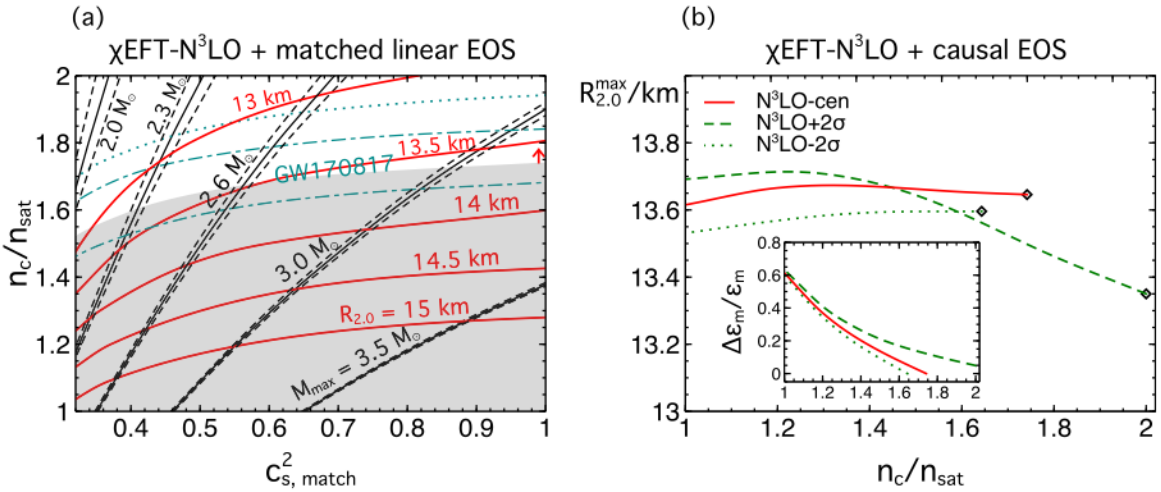

FIG. 6. Panel (a) shows $R_{2.0}$ and $M_{\rm max}$ contours on the $(c^2_{s,\rm match}, n_c)$ plane, obtained without a phase transition in the density interval $n_{\rm B} = (1\text{–}2)\,n_{\rm sat}$. For each value of $M_{\rm max}$, the central solid curves represent results with N^{3}LO-cen; dashed lines indicate $\pm1\sigma$ bounds. For $R_{2.0}$ contours, only results with N^{3}LO-cen are shown (red solid lines). The gray-shaded region is excluded by the binary tidal deformability constraint $\tilde{\Lambda}_{1.186} \leqslant 720$ from GW170817 at the 90% credibility level [45] if N^{3}LO-cen is assumed; the (cyan) dot-dashed lines refer to constraints with the $\pm1\sigma$ uncertainties. The thin dotted line indicates an even lower upper bound with N^{3}LO-cen and $\tilde{\Lambda}_{1.186} \leqslant 600$. Panel (b) shows maximally allowed value of $R_{2.0}$ that is compatible with $\tilde{\Lambda}_{1.186} \leqslant 720$ by matching to the causal EOS with a density discontinuity $\Delta\varepsilon_{\rm m}/\varepsilon_{\rm m} \geqslant 0$ (shown in the inset) at $n_c = (1\text{–}2)\,n_{\rm sat}$, below which the N^{3}LO-cen and $\pm2\sigma$ EOSs are used. The value of $R^{\rm max}_{2.0}$ associated with the highest n_c on each curve, represented by the open diamonds, corresponds to the intersection points between the upper y axis and the boundary of the gray region in Figs. 2 and 4. Note, however, that these extremely large $R_{2.0}$ are also indicative of very high maximum masses $\gtrsim 2.8\,{\rm M}_\odot$ [see panel (a) for an estimate], above the secondary component mass of GW190814 [52].

plane. It is obvious that a finite density discontinuity $\Delta\varepsilon_{\rm m}$ at the phase transition is effective in accommodating GW170817 owing to the preferable softening, but, correspondingly, the necessity for increasing $c^2_{s,\rm max}$ at higher densities is inevitably strengthened, leading to sizable corrections to the $\min\{c^2_{s,\rm max}\}$ indicated from the previous green curves inside the gray regions of Fig. 4 (which assumed no phase transition).

In essence, introducing sharp phase transitions in the EOS between $n_{\rm B} = (1\text{–}2)\,n_{\rm sat}$ has three principal outcomes: (i) it is now possible for small matching densities $n_c \lesssim 1.4\text{–}1.6\,n_{\rm sat}$ to be compatible with GW170817 provided that the corresponding discontinuity in energy density is sufficiently large; (ii) depending on the specified value of n_c, the binary tidal deformability upper bound $\tilde{\Lambda}_{1.186} = 720$ now translates into different GW170817 boundaries (see Fig. 5) on the $R_{2.0}$-$c^2_{s,\rm match}$ plane; (iii) the lower bound on the core speed of sound $\min\{c^2_{s,\rm max}\}$ (to satisfy large $M_{\rm max}$ and/or large $R_{2.0}$) increases due to the added softening of EOS at low densities.

Our results indicate that, to satisfy both small tidal deformabilities of GW170817 and $R_{2.0} \geqslant 13$ km, the conservative lower bounds [see Fig. 5(b)] on the minimum core speed of sound should be $\min\{c^2_{s,\rm max}\} \geqslant 0.442\,(0.411)$ and $R^{\rm max}_{2.0} \approx 13.35$ km (13.46 km), if χEFT-N^{3}LO is assumed valid up to $n_c = 2.0\,n_{\rm sat}$ $(1.8\,n_{\rm sat})$. In contrast, the values previously inferred without taking into account GW170817 constraints were $\min\{c^2_{s,\rm max}\} \geqslant 0.42\,(0.35)$ and $R^{\rm max}_{2.0} \approx 13.53$ km (13.87 km), respectively [see discussion in Sec. III A and Fig. 4(b)]. Similarly, for a smaller lower bound $R_{2.0} \geqslant 12.5$ km, Fig. 5(b) indicates that $\min\{c^2_{s,\rm max}\} \geqslant 0.348\,(0.333)$ for $n_c = 2.0\,n_{\rm sat}$ $(1.8\,n_{\rm sat})$.

It is worth noting that, although there is still a chance for the conformal limit $\min\{c^2_{s,\rm max}\} \leqslant 1/3$ to be compatible with $M_{\rm max} \geqslant 2.0\,{\rm M}_\odot$ and GW170817 [the small triangular region in Figs. 5(a) and 5(b) encompassed by the rightmost blue curve, bottom black solid curve, and bottom horizontal dotted line], the permitted range of $R_{2.0}$ is quite narrow, i.e., $R_{2.0} = (11.55 - 13.00)$ km for χEFT-N^{3}LO at the 2σ confidence level. Moreover, a slight increase in $M_{\rm max} \gtrsim 2.1\,{\rm M}_\odot$ would suffice to exclude $\min\{c^2_{s,\rm max}\} \leqslant 1/3$ [25].

Figure 6(b) shows the absolute upper bounds on $R_{2.0}$ imposed by causality and GW170817 with varying n_c. We find that $R^{\rm max}_{2.0}$ is relatively insensitive to n_c, except for the stiffest N^{3}LO + 2σ EOS. The inset depicts the corresponding phase-transition strengths $\Delta\varepsilon_{\rm m}/\varepsilon_{\rm m}$ at different matching densities, where $\varepsilon_{\rm m}$ is the energy density in the χEFT EOS at $n_{\rm B} = n_c$. Values of $R^{\rm max}_{2.0}$ reached at the highest n_c (and simultaneously the smallest $\Delta\varepsilon_{\rm m}/\varepsilon_{\rm m}$) are denoted by the open diamonds, which also correspond to where the upper y axis intersects with the boundary of the gray regions in Figs. 2 and 4. It is reasonably justified to claim that, regardless of the presence or absence of unusual softening in the EOS at low densities $(1\text{–}2)\,n_{\rm sat}$, the largest achievable radius for a $\approx 2\,{\rm M}_\odot$ neutron star is $R^{\rm max}_{2.0} \approx 13.7$ km, limited by causality and GW170817. Note that this is close to the central value reported in Ref. [3] (see also the top panel in Fig. 2); should future observations confirm $R_{2.0}$ greater than 13.7 km, it would strongly favor a transition at subsaturation density to an EOS that is significantly stiffer than predicted by χEFT calculations.

We also display in Fig. 6(a) how both $M_{\rm max}$ and $R_{2.0}$ depend on n_c (chosen to lie within $1\text{–}2\,n_{\rm sat}$) and $c^2_{s,\rm match}$ at high

densities, assuming the validity of χEFT-N^{3}LO up to n_c and $\Delta\varepsilon_{\rm m} = 0$. Because finite $\Delta\varepsilon_{\rm m}$ would only reduce both $M_{\rm max}$ and $R_{2.0}$, the values of $c^2_{s,{\rm match}}$ indicated from Fig. 6(a) by imposing lower bounds on $M_{\rm max}$ or $R_{2.0}$ serve as conservative estimates for $\min\{c^2_{s,{\rm max}}\}$. We find that $\min\{c^2_{s,{\rm max}}\}$ is in general more sensitive to $R_{2.0}$ than to $M_{\rm max}$: an increase in $R_{2.0}$ from 13.0 to 13.5 km is more constraining than an increase in $M_{\rm max}$ from 2.0 $\mathrm{M}_\odot$ to 2.3 $\mathrm{M}_\odot$, pushing $\min\{c^2_{s,{\rm max}}\}$, e.g., from $\approx$0.46 to $\approx$0.80 in the former case compared with $\approx$0.33 to $\approx$0.45 in the latter case for $n_c = 1.75\,n_{\rm sat}$. We emphasize that $M_{\rm max}$ contours (and $R_{2.0}$ contours) in Fig. 6(a) should be viewed as lower bounds only, and no phase transitions were assumed because otherwise the required $\min\{c^2_{s,{\rm max}}\}$ are always higher.

Despite different inference methods used, recent works applying *NICER* measurements of PSR J0740 + 6620 to extract neutron-star properties and EOS constraints obtained results that are broadly consistent [28,53–55]. The N^{3}LO + 2σ EOS in the outer core used in this work is relatively stiff at $n_{\rm B} \gtrsim n_{\rm sat}$ compared with the χEFT models applied in Refs. [53,54] (see also Fig. 6 in Ref. [53] for a comparison), and its pressure coincides with the mean value inferred from theory-agnostic study in Ref. [28] at $2\,n_{\rm sat}$ as shown in Fig. 1. Hence, we expect our estimates on $\min\{c^2_{s,{\rm max}}\}$ to be conservative. Given the still large uncertainties involved, the consensus is that current combined data from GW, x-ray, and radio observations are not yet informative enough to identify or rule out microscopic models that exhibit first-order or crossover transitions into exotic matter at densities relevant for neutron stars (for different phase-transition scenarios explored, see, e.g., Refs. [56–62]). We investigated in detail the enhancement in $\min\{c^2_{s,{\rm max}}\}$ to reach large $R_{2.0}$ when the EOS undergoes a finite discontinuity $\Delta\varepsilon_{\rm m}$ at low densities, limited by the small tidal deformabilities measured in GW170817. The possibility of phase transitions in the density interval $(1\text{–}2)\,n_{\rm sat}$ is of particular interest for experimental probes such as low-to-intermediate heavy-ion collisions [63], as existing analyses of these experiments have largely been done with nucleonic degrees of freedom only.

Earlier work has revealed that multimessenger observations of GW170817 provided additional constraints on the NS maximum mass $M_{\rm max} \lesssim 2.3\,\mathrm{M}_\odot$ [64–68]. Future GW analyses of binary neutron-star and black hole-neutron star mergers hold the promise of deriving a more definite upper bound on $M_{\rm max}$, if their concomitant electromagnetic (EM) signals are to be detected. Nevertheless, a lower value for $M_{\rm max}$ between 2.0–2.3 $\mathrm{M}_\odot$ does not improve the lower bound on the sound speed because a phase transition at supranuclear density can easily accommodate it.

IV. SUMMARY AND OUTLOOK

In this article, we have addressed how nuclear physics constraints on the EOS of matter at the moderate densities encountered in the neutron-star outer core can be combined with recent *NICER* observations to provide a lower bound on the maximum speed of sound in dense QCD. We employed recent χEFT calculations of the nuclear EOS up to N^{3}LO with EFT truncation errors quantified to explore the implications of the large inferred radius of PSR J0740 + 6620—the heaviest of the precisely measured two-solar mass neutron stars. We found that the minimum required value for the highest sound speed reached in the inner core increases rapidly with the radius of massive neutron stars.

If χEFT is an efficient expansion for nuclear interactions at $n_{\rm B} \lesssim 2\,n_{\rm sat}$, a lower limit on $R_{2.0} > 12.5$ km indicates $c_s^2 \gtrsim 0.36$ in the inner core, and this lower bound is very sensitive to $R_{2.0}$. For $R_{2.0} = 13.1$ km, we found that $\min\{c^2_{s,{\rm max}}\} = 1.0$ when we used the central values for the χEFT EOS (see Fig. 2), and $\min\{c^2_{s,{\rm max}}\} = 0.5$ for the stiffest EOS compatible with χEFT at the 2σ level [see Fig. 4(b)]. Together with the predictions of perturbative QCD at asymptotically high densities ($\gtrsim 40\,n_{\rm sat}$), this implies that the speed of sound must be a nonmonotonic function of density, with at least two extrema [17,69]. If χEFT constraints are used at densities $\lesssim 1.5\,n_{\rm sat}$ only, it is possible to accommodate a scenario in which the sound speed is a monotonic function of density. However, in this case, the sound speed must increase very rapidly to its asymptotic value of $c_s = 1/\sqrt{3}$ within the neutron star. More significantly, the results in Fig. 5 indicate that a monotonically increasing sound speed in QCD implies that $M_{\rm max} \lesssim 2.1\,\mathrm{M}_\odot$ and $R_{2.0} \lesssim 13$ km.

Our conclusion that the large inferred radius of PSR J0740 + 6620 favors high sound speed is further strengthened by several other calculations of the EOS, which are based on phenomenological models of NN interactions constrained by scattering data and simple models for $3N$ interactions [70–72]. Generically, these models predict smaller pressure as well as smaller speed of sound values at $n_{\rm B} \lesssim 2\,n_{\rm sat}$ compared with the stiffest EOS compatible with χEFT. A common feature shared by these models and χEFT is the important role of repulsive $3N$ forces. We find that, even in phenomenological models with strong $3N$ forces, $R_{2.0} > 13$ km can only be accessed if $\min\{c^2_{s,{\rm max}}\} > 0.5$.

For EOS calculations based on χEFT, it is important to explore EFT truncation errors at high densities for a wide range of potentials as well as the regulator dependence further. In particular, a full Bayesian analysis of the nuclear EOS in which also the uncertainties from the low-energy couplings in the nuclear interactions (in addition to the EFT truncation error) are quantified is required. This will lead to the development of improved order-by-order chiral NN and $3N$ potential up to N^{3}LO with uncertainties rigorously quantified. An important step toward this goal has recently been achieved in Ref. [73], where a set of order-by-order chiral NN and $3N$ interactions with theoretical uncertainties fully quantified has been constructed up to N^{2}LO. Detailed comparison with the predictions of χEFT with Δ baryons could also provide valuable insights [74–76].

Our findings underscore the need to improve constraints on the EOS of neutron-rich matter in the density region $n_{\rm B} \approx (1\text{–}2)\,n_{\rm sat}$. It is fortuitous that both theory and experiment can access these densities in the next five to ten years. Efforts to test and constrain χEFT predictions at densities $n_{\rm B} \simeq n_{\rm sat}$ using neutron-rich nuclei as probes, including improved measurements of neutron-skin thicknesses and dipole polarizabilities, would be valuable and are anticipated in the near-term future [77,78]. Heavy-ion experiments that study collisions of neutron-rich nuclei at intermediate energy can

provide guidance for the behavior of the EOS in the density regime of (1–2) $n_{\rm sat}$ [63,79–81]. For these reasons, the density range $n_{\rm B} \approx (1\text{–}2)\, n_{\rm sat}$ is emerging to be the *golden window* of neutron-star physics, in which we can expect significant advances across multiple disciplines soon.

When combined with improved astrophysical constraints on the radius of massive neutron stars, these developments can significantly tighten the lower bound on the maximum speed of sound; especially if the inferred radius is large. From Fig. 2, we infer that a stringent lower bound on the radius $R_{2.0} > 13$ km would require that $c_s^2 \geqslant 0.56$ and the existence of a region where c_s^2 increases dramatically with density. Such matter would be quite distinct from neutron-rich matter in the outer core, or weakly interacting quark matter. In contrast, if the inferred radius is in the range of 11.5–12.5 km, the resulting bound on the minimum sound speed in the core would be less restrictive and compatible with $c_s^2 \lesssim 1/3$ [17,18].

The difference between the extracted radii obtained by the two independent analyses in Refs. [3,4] suggests that a theory-informed prior for the neutron-star radii can improve the precision of these analyses. In particular, we can anticipate that χEFT-based predictions for viable neutron-star radii as discussed in Ref. [25] will usefully reduce the radius posterior uncertainties when employed as priors for astrophysical modeling efforts. In future work, these physically motivated priors could be used in joint analyses of GW170817 and *NICER* data to obtain more stringent constraints on the maximum speed of sound in the core, the neutron-star radius, and its tidal deformability.

ACKNOWLEDGMENTS

We thank Constantinos Constantinou, Cole Miller, and Madappa Prakash for sharing their insights with us and are grateful to the National Science Foundation's *Physics Frontier Center: The Network for Neutrinos, Nuclear Astrophysics, and Symmetries* (N3AS) for encouragement and support. This material is based upon work supported by the U.S. Department of Energy, Office of Science, Office of Nuclear Physics, under the FRIB Theory Alliance Award No. DE-SC0013617. S.H. was supported by the National Science Foundation, Grant No. PHY-1630782, and the Heising-Simons Foundation, Grant No. 2017-228. The work of S.R. was supported by the U.S. Department of Energy under Grant No. DE-FG02-00ER41132.

[1] H. T. Cromartie *et al.*, Nat. Astron. **4**, 72 (2019).
[2] E. Fonseca *et al.*, Astrophys. J. Lett. **915**, L12 (2021).
[3] M. C. Miller *et al.*, Astrophys. J. Lett. **918**, L28 (2021).
[4] T. E. Riley *et al.*, Astrophys. J. Lett. **918**, L27 (2021).
[5] P. Demorest, T. Pennucci, S. Ransom, M. Roberts, and J. Hessels, Nature (London) **467**, 1081 (2010).
[6] J. Antoniadis *et al.*, Science **340**, 6131 (2013).
[7] B. P. Abbott *et al.* (LIGO Scientific, Virgo), Phys. Rev. Lett. **121**, 161101 (2018).
[8] S. De, D. Finstad, J. M. Lattimer, D. A. Brown, E. Berger, and C. M. Biwer, Phys. Rev. Lett. **121**, 091102 (2018); **121**, 259902(E) (2018).
[9] C. D. Capano, I. Tews, S. M. Brown, B. Margalit, S. De, S. Kumar, D. A. Brown, B. Krishnan, and S. Reddy, Nat. Astron. **4**, 625 (2020).
[10] T. Zhao and J. M. Lattimer, Phys. Rev. D **98**, 063020 (2018).
[11] P. Landry, R. Essick, and K. Chatziioannou, Phys. Rev. D **101**, 123007 (2020).
[12] M. Al-Mamun, A. W. Steiner, J. Nättilä, J. Lange, R. O'Shaughnessy, I. Tews, S. Gandolfi, C. Heinke, and S. Han, Phys. Rev. Lett. **126**, 061101 (2021).
[13] F. Özel and P. Freire, Annu. Rev. Astron. Astrophys. **54**, 401 (2016).
[14] S. Bogdanov, C. O. Heinke, F. Özel, and T. Güver, Astrophys. J. Lett. **831**, 184 (2016).
[15] A. W. Steiner, J. M. Lattimer, and E. F. Brown, Eur. Phys. J. A **52**, 18 (2016).
[16] A. W. Steiner, C. O. Heinke, S. Bogdanov, C. Li, W. C. G. Ho, A. Bahramian, and S. Han, Mon. Not. R. Astron. Soc. **476**, 421 (2018).
[17] P. Bedaque and A. W. Steiner, Phys. Rev. Lett. **114**, 031103 (2015).
[18] I. Tews, J. Carlson, S. Gandolfi, and S. Reddy, Astrophys. J. Lett. **860**, 149 (2018).
[19] C. Drischler, K. Hebeler, and A. Schwenk, Phys. Rev. Lett. **122**, 042501 (2019).
[20] M. Leonhardt, M. Pospiech, B. Schallmo, J. Braun, C. Drischler, K. Hebeler, and A. Schwenk, Phys. Rev. Lett. **125**, 142502 (2020).
[21] C. Drischler, R. J. Furnstahl, J. A. Melendez, and D. R. Phillips, Phys. Rev. Lett. **125**, 202702 (2020).
[22] C. Drischler, J. A. Melendez, R. J. Furnstahl, and D. R. Phillips, Phys. Rev. C **102**, 054315 (2020).
[23] J. A. Melendez, R. J. Furnstahl, D. R. Phillips, M. T. Pratola, and S. Wesolowski, Phys. Rev. C **100**, 044001 (2019).
[24] C. Drischler, J. W. Holt, and C. Wellenhofer, Annu. Rev. Nucl. Part. Sci. **71**, 403 (2021).
[25] C. Drischler, S. Han, J. M. Lattimer, M. Prakash, S. Reddy, and T. Zhao, Phys. Rev. C **103**, 045808 (2021).
[26] K. Hebeler, J. Lattimer, C. Pethick, and A. Schwenk, Astrophys. J. **773**, 11 (2013).
[27] D. Lonardoni, I. Tews, S. Gandolfi, and J. Carlson, Phys. Rev. Research **2**, 022033(R) (2020).
[28] I. Legred, K. Chatziioannou, R. Essick, S. Han, and P. Landry, Phys. Rev. D **104**, 063003 (2021).
[29] C. Constantinou, B. Muccioli, M. Prakash, and J. M. Lattimer, Phys. Rev. C **89**, 065802 (2014).
[30] A. S. Schneider, C. Constantinou, B. Muccioli, and M. Prakash, Phys. Rev. C **100**, 025803 (2019).
[31] J. W. Negele and D. Vautherin, Nucl. Phys. A **207**, 298 (1973).
[32] G. Baym, C. Pethick, and P. Sutherland, Astrophys. J. **170**, 299 (1971).
[33] C. Drischler, V. Somà, and A. Schwenk, Phys. Rev. C **89**, 025806 (2014).
[34] C. Drischler, K. Hebeler, and A. Schwenk, Phys. Rev. C **93**, 054314 (2016).
[35] N. Kaiser, Phys. Rev. C **91**, 065201 (2015).

[36] C. Wellenhofer, J. W. Holt, and N. Kaiser, Phys. Rev. C **93**, 055802 (2016).
[37] R. Somasundaram, C. Drischler, I. Tews, and J. Margueron, Phys. Rev. C **103**, 045803 (2021).
[38] P. Wen and J. W. Holt, Phys. Rev. C **103**, 064002 (2021).
[39] I. Tews, T. Krüger, K. Hebeler, and A. Schwenk, Phys. Rev. Lett. **110**, 032504 (2013).
[40] T. Krüger, I. Tews, K. Hebeler, and A. Schwenk, Phys. Rev. C **88**, 025802 (2013).
[41] C. Drischler, A. Carbone, K. Hebeler, and A. Schwenk, Phys. Rev. C **94**, 054307 (2016).
[42] B. T. Reed, F. J. Fattoyev, C. J. Horowitz, and J. Piekarewicz, Phys. Rev. Lett. **126**, 172503 (2021).
[43] P.-G. Reinhard, X. Roca-Maza, and W. Nazarewicz, Phys. Rev. Lett. **127**, 232501 (2021).
[44] J. Piekarewicz, Phys. Rev. C **104**, 024329 (2021).
[45] B. P. Abbott *et al.* (LIGO Scientific Collaboration and Virgo Collaboration), Phys. Rev. X **9**, 011001 (2019).
[46] R. C. Tolman, Phys. Rev. **55**, 364 (1939).
[47] J. Oppenheimer and G. Volkoff, Phys. Rev. **55**, 374 (1939).
[48] J. M. Lattimer and M. Prakash, Science **304**, 536 (2004).
[49] P. Haensel, J. L. Zdunik, M. Bejger, and J. M. Lattimer, Astron. Astrophys. **502**, 605 (2009).
[50] A. Cherman, T. D. Cohen, and A. Nellore, Phys. Rev. D **80**, 066003 (2009).
[51] T. Dietrich, S. Khan, R. Dudi, S. J. Kapadia, P. Kumar, A. Nagar, F. Ohme, F. Pannarale, A. Samajdar, S. Bernuzzi, G. Carullo, W. Del Pozzo, M. Haney, C. Markakis, M. Purrer, G. Riemenschneider, Y. E. Setyawati, K. W. Tsang, and C. Van Den Broeck, Phys. Rev. D **99**, 024029 (2019).
[52] R. Abbott *et al.* (LIGO Scientific, Virgo), Astrophys. J. Lett. **896**, L44 (2020).
[53] G. Raaijmakers, S. K. Greif, K. Hebeler, T. Hinderer, S. Nissanke, A. Schwenk, T. E. Riley, A. L. Watts, J. M. Lattimer, and W. C. G. Ho, Astrophys. J. Lett. **918**, L29 (2021).
[54] P. T. H. Pang, I. Tews, M. W. Coughlin, M. Bulla, C. Van Den Broeck, and T. Dietrich, Astrophys. J. **922**, 14 (2021).
[55] B. Biswas, Astrophys. J. **921**, 63 (2021).
[56] R. Somasundaram and J. Margueron, arXiv:2104.13612.
[57] T. Zhao and J. M. Lattimer, Phys. Rev. D **102**, 023021 (2020).
[58] S. Han and M. Prakash, Astrophys. J. Lett. **899**, 164 (2020).
[59] S.-P. Tang, J.-L. Jiang, M.-Z. Han, Y.-Z. Fan, and D.-M. Wei, Phys. Rev. D **104**, 063032 (2021).
[60] H. Tan, T. Dore, V. Dexheimer, J. Noronha-Hostler, and N. Yunes, Phys. Rev. D **105**, 023018 (2022).
[61] J. J. Li, A. Sedrakian, and M. Alford, Phys. Rev. D **104**, L121302 (2021).
[62] J.-E. Christian and J. Schaffner-Bielich, arXiv:2109.04191.
[63] P. Danielewicz, R. Lacey, and W. G. Lynch, Science **298**, 1592 (2002).
[64] B. Margalit and B. D. Metzger, Astrophys. J. Lett. **850**, L19 (2017).
[65] M. Shibata, E. Zhou, K. Kiuchi, and S. Fujibayashi, Phys. Rev. D **100**, 023015 (2019).
[66] M. Ruiz, S. L. Shapiro, and A. Tsokaros, Phys. Rev. D **97**, 021501(R) (2018).
[67] L. Rezzolla, E. R. Most, and L. R. Weih, Astrophys. J. Lett. **852**, L25 (2018).
[68] B. P. Abbott *et al.* (LIGO Scientific, Virgo), Classical Quantum Gravity **37**, 045006 (2020).
[69] I. Tews, J. Margueron, and S. Reddy, Phys. Rev. C **98**, 045804 (2018).
[70] A. Akmal, V. R. Pandharipande, and D. G. Ravenhall, Phys. Rev. C **58**, 1804 (1998).
[71] S. C. Pieper, V. R. Pandharipande, R. B. Wiringa, and J. Carlson, Phys. Rev. C **64**, 014001 (2001).
[72] S. Gandolfi, J. Carlson, and S. Reddy, Phys. Rev. C **85**, 032801(R) (2012).
[73] S. Wesolowski, I. Svensson, A. Ekström, C. Forssén, R. J. Furnstahl, J. A. Melendez, and D. R. Phillips, Phys. Rev. C **104**, 064001 (2021).
[74] A. Ekström, G. Hagen, T. D. Morris, T. Papenbrock, and P. D. Schwartz, Phys. Rev. C **97**, 024332 (2018).
[75] M. Piarulli, I. Bombaci, D. Logoteta, A. Lovato, and R. B. Wiringa, Phys. Rev. C **101**, 045801 (2020).
[76] W. G. Jiang, A. Ekström, C. Forssén, G. Hagen, G. R. Jansen, and T. Papenbrock, Phys. Rev. C **102**, 054301 (2020).
[77] D. Becker *et al.*, Eur. Phys. J. A **54**, 208 (2018).
[78] D. Budker, J. R. C. López-Urrutia, A. Derevianko, V. V. Flambaum, M. W. Krasny, A. Petrenko, S. Pustelny, A. Surzhykov, V. A. Yerokhin, and M. Zolotorev, Ann. Phys. (Berlin, Ger.) **532**, 2000204 (2020).
[79] J. Estee *et al.* (SπRIT), Phys. Rev. Lett. **126**, 162701 (2021).
[80] S. Huth, P. T. H. Pang, I. Tews, T. Dietrich, A. L. Fèvre, A. Schwenk, W. Trautmann, K. Agarwal, M. Bulla, M. W. Coughlin, and C. Van Den Broeck, arXiv:2107.06229.
[81] FRIB Science Community, The scientific case for the 400 MeV/u energy upgrade of FRIB, (2021), https://frib.msu.edu/_files/pdfs/frib400_final.pdf.